This is the accepted manuscript made available via CHORUS. The article has been published as:

Effective gyration of polar vortex arrays controlled by high orbital angular momentum of light

Lingyuan Gao, Sergei Prokhorenko, Yousra Nahas, and Laurent Bellaiche

Phys. Rev. B **109**, L121110 — Published 15 March 2024

DOI: 10.1103/PhysRevB.109.L121110

Effective gyration of polar vortex arrays controlled by high orbital angular momentum of light

Lingyuan Gao,[1] Sergei Prokhorenko,[1] Yousra Nahas,[1] and Laurent Bellaiche[1]

[1] *Physics Department and Institute for Nanoscience and Engineering, University of Arkansas, Fayetteville, Arkansas, 72701, USA*

(Dated: February 28, 2024)

The electric field of the optical vortex (OV) beam displays a specific winding pattern determined by its spatial variation and angular momentum. OV beam can serve as a optical spanner, which exerts a force torque to rotate particles around the beam axis. In this work, using first-principles-based calculations, we demonstrate that an OV beam with high orbital angular momentum (OAM) can induce local electric dipoles to self-order and form a vortex array distributed along azimuthal directions. More importantly, owing to its intrinsic symmetry, the evolution of vortex array with time can be viewed as an effective spinning around the central axis, while its rotation speed is also connected to the OAM value. Our study thus presents an alternative approach for manipulating polar vortices using optical field apart from mechanical and electric stimulus, and especially for a deterministic control of vortex dynamics that is critical in application of memory devices.

Light beams established on Laguerre-Gaussian (LG) mode set was invented in laboratory by Allen *et al.* more than three decades ago [1]. Such beams carry an orbital angular momentum (OAM) defined by the phase factor $e^{im\phi}$, where ϕ is the azimuthal angle, and m is an integer associated to photon's OAM $m\hbar$. In addition to the helical wave front denoted by $e^{im\phi}$, LG beams are characterized by an annular profile of the light intensity $(\frac{r}{w})^{|m|}e^{-\frac{r^2}{w^2}}$. As a result, the intensity gradient along the radial direction generates a "gradient force" that drives small particles to move towards the beam focus, while the phase gradient along the azimuthal angle direction generates a "scattering force" that can circulate particles on the annular ring of LG beams via light absorption [2–5]. Therefore, LG beams are also known as "optical tweezer" or "optical spanner", as they can manipulate motion of particles ranging from nanometers to micrometers [6, 7].

For a circularly-polarized LG light beam, its two-dimensional (2D) electric or magnetic field is naturally endowed with a winding number $-m \cdot \sigma$, where σ denotes the helicity of the light [8]. The winding number, as an integer, quantifies the number of times the vector field completes a rotation of 2π as it encircles the center of the beam, where the intensity of the field is zero and the direction of the field cannot be defined [9]. This singularity, together with the entire whirling configuration, presents the field as an $SO(2)$"optical vortex" (OV), which cannot be smoothly deformed into a linearly-polarized light, and is commonly recognized as a topological defect in two-dimensional (2D) space [10, 11]. The vortex-like structures manifest in various exotic phases and condensed matter systems, including superfluid, superconductors and magnetic media [12–15]. Rapid progress has also been made in exploring ferroelectric vortices built by electric dipoles. They were theoretically predicted in ferroelectric nanodisks and nanodots in early 2000s [16, 17], and were not revealed in experiment until 2016: Yadav *et al.* showed ordered arrays of vortex pairs formed in $PbTiO_3/SrTiO_3$ [18], which later exhibited fascinating phenomena such as emergent chirality and negative capacitance [19, 20]. Different from the Dzyaloshinsky-Moriya interaction rising from the interplay between spin orbit coupling and superexchange in magnetic systems [21, 22], the complex dipolar textures in ferroelectrics emerge from the competition between electrostatic, elastic and gradient energies [23, 24].

One critical step of utilizing polar vortices in applications is to robustly handle vortices with external control. Experiments have shown that by applying electric field, conversion between vortex and stripe phases [25], and a reversal of chirality in polar vortices [26], can be achieved. Beyond static electric field, subpicosecond light pulses with above-bandgap-excitation can convert vortex array into supercrystals [27]; THz field can drive collective sub-THz dynamics of polar vortices, such as a transverse oscillation at 0.08 THz [28, 29]. However, to the best of our knowledge, how to move polar vortices in a controllable manner still remains unknown.

In this work, using atomistic simulations based on first principles calculations, we validate the idea of converting optical vortices to dynamical polar vortices, by making the unique optical field–LG beams at THz frequency to interact with ferroelectric materials. Intringuingly, the beam does not only induce the formation of polar vortices, but also manipulates their motion in a controllable way. For specific OAM value m, the winding pattern of the electric field exhibits an symmetrical profile, and its coupling with electric dipoles gives rise to the formation of a polar vortex array in ferroelectric ultrathin films. Vortices with opposite chirality are positioned next to each other on an annular ring, and their configurations evolve with the time-dependent field. This can be equivalently viewed as a spinning of the whole vortex array around the beam center at the same frequency of the THz optical field, which we call as "effective gyration".

Electric field of LG beam The electric field of LG beam can be generally described as:

$$\vec{E}(r,\phi,z=0) = E_0\ C_{lm}\frac{1}{w}(\frac{\sqrt{2}r}{w})^{|m|}e^{-\frac{r^2}{w^2}}L_l^{|m|}(\frac{2r^2}{w^2}) \\ \big(\cos(m\phi-\omega t)\vec{e}_x - \sigma\sin(m\phi-\omega t)\vec{e}_y\big). \quad (1)$$

In the equation above, E_0 and w denote the magnitude and beam radius of the electric field, respectively. C_{lm} is the normalization constant, $L_l^{|m|}$ is the generalized Laguerre polynomial, and l is the node index. Here we adopt $\sigma = +1$ to fix the helicity as left-polarized.

We first examine fields with $l = 0$. In this instance, $C_{lm} = 1$ is a constant. Figures 1(a)-(c) illustrate the field configuration when $m = -2, -3, -4$ at $t = pT$ (where p is a positive integer and T denotes the period of the field). To have a better contrast between the field (Figs. 1(a)-(e)) and the response of on-site dipoles (Figs. 1(f)-(j)), we plot both fields and dipoles in the dimension of the simulation supercell (introduced below). There is only one radial node (namely, the local maximum intensity is on a ring with a radius of $\sim\sqrt{2}w$), and the field magnitude decreases radially from the ring in both the inward and outward directions. At the center (the origin of the cylindrical coordinates), E decreases to zero. At $t = pT$, according to Eq. 1, the orientation of the field at (r,ϕ) is fully determined by its azimuthal angle ϕ, and the extent of $\vec{E}(r,\phi)$'s rotation increases with the OAM magnitude $|m|$. In particular, for fields radially oriented towards to or away from the center of the beam, their azimuthal angles are given by:

$$-m\phi_{\text{in}} = \phi_{\text{in}} + (2n-1)\cdot\pi, \\ -m\phi_{\text{out}} = \phi_{\text{out}} + (2n)\cdot\pi. \quad (2)$$

In the equation above, n is an integer, and we use subscripts "in" and "out" to denote the flowing direction of the field. As shown in the plot, lines oriented along $\phi_{\text{in}} = \frac{(2n-1)\cdot\pi}{(-m-1)}$ and $\phi_{\text{out}} = \frac{2n\cdot\pi}{(-m-1)}$ separate the whole plane into several subregions: in each subregion, the outgoing fields flow away from the center along one boundary (ϕ_{out}), adjust their orientations along the contour, and flow towards the center along the other boundary (ϕ_{in}) to form a flux-closure domain. Symmetry-wise, in a 2D field, these lines serve as symmetry axes, relative to which reflection operations can be performed between these domains. In addition to reflection, two-fold and three-fold rotations can also map one domain to another in Figs. 1(b)(c), indicating field patterns there belonging to two-dimensional D_2 and D_3 groups, respectively. Note in Eq. 2, no solution exists for $m = -1$; this is due to the fact that the change of the field orientation for $m = -1$ cannot exceed 2π even making a full contour. Thus, symmetric subregions fail to develop, leading the field to exhibit varied shapes at different t [30].

We next examine cases when the field pattern is more complicated: (1) for $m > 0$, symmetric subregions form for all m (including $m = 1$) with a symmetry of $C_{m+1,v}$, while each subregion is an open-flux domain: the field flows in along one boundary (ϕ_{in}), but exhibits an anti-crossing behavior at the center, and flows out along the other boundary (ϕ_{out}). Similar to $m < 0$, $\phi_{\text{in}} = \frac{(2n-1)\cdot\pi}{(m+1)}$ and $\phi_{\text{out}} = \frac{2n\cdot\pi}{(m+1)}$ can be easily derived for $m > 0$. (2) For $l > 0$, along the radial direction, there are $l+1$ nodes with the local maximal intensity and l nodes with zero field intensity, resulting in the formation of l bright annular rings. We illustrate these two cases with $l = 0, m = 3$ and $l = 1, m = -3$ in Figs. 1(d)(e), respectively.

The intriguing field patterns of LG beams enlighten us to consider writing such symmetric optical textures in real materials. An active response from the material to local optical field at a microscopic level is required to achieve such goal. Order parameters such as electric dipoles or magnetic moments, reside continuously on lattices over a long range and respond to optical fields promptly, naturally fulfilling this criterion. Former studies investigated the response of magnetic materials to magnetic fields of LG beams [31–33]; here, we do not focus on magnetic compounds but rather on non-magnetic, ferroelectric materials, where the response to electric field part is more crucial.

Polar vortex array induced by LG beam Experimentally observed polar vortex is at a scale of tens of unit cells [18]. Therefore, we choose the prototype ferroelectric ultrathin films $Pb(Zr_{0.4}Ti_{0.6})O_3$ (PZT) in the $80\times80\times5$ supercell grown along [001] direction as the modelling system, where each unit cell has a lattice constant of 0.4 nm. The unit of a polar vortex is an on-site electric dipole $\boldsymbol{p}_i$ in cell i, essentially representing an off-centering ion displacement $\boldsymbol{u}_i$. In ferroelectric phase transition, such displacements rise from the condensation of soft modes. Therefore, we adopt the effective Hamiltonian computational approach, which defines a restricted Born-Oppenheimer potential energy surface with soft modes and acoustic modes fitted from first principles calculations [34–36]. The method demonstrated remarkable success in predicting diverse exotic polar structures characterized by atomic distortions in PZT systems [17, 37–44]. We perform molecular dynamics simulations to explore the potential energy landscape and all possible dipolar configurations when electric field of LG beam is introduced in a continuous wave form to a well-equilibrated monodomain configuration at 10 K: with all dipoles aligning along $[00\bar{1}]$—the out-of-plane z direction, we let the light propagate along z axis, so that the electric field, which only has in-plane x, y components, interacts with the in-plane part of dipoles. The polarization magnitude in poled monodomain is computed to be 73 $\mu C/cm^2$, close to experimental measurements [45–47]. Considering the dimension of the system and the response time of soft modes, we choose $w = 5$ unit cells (u.c.) and $\omega = 1$ THz as the beam radius and light frequency, respectively.

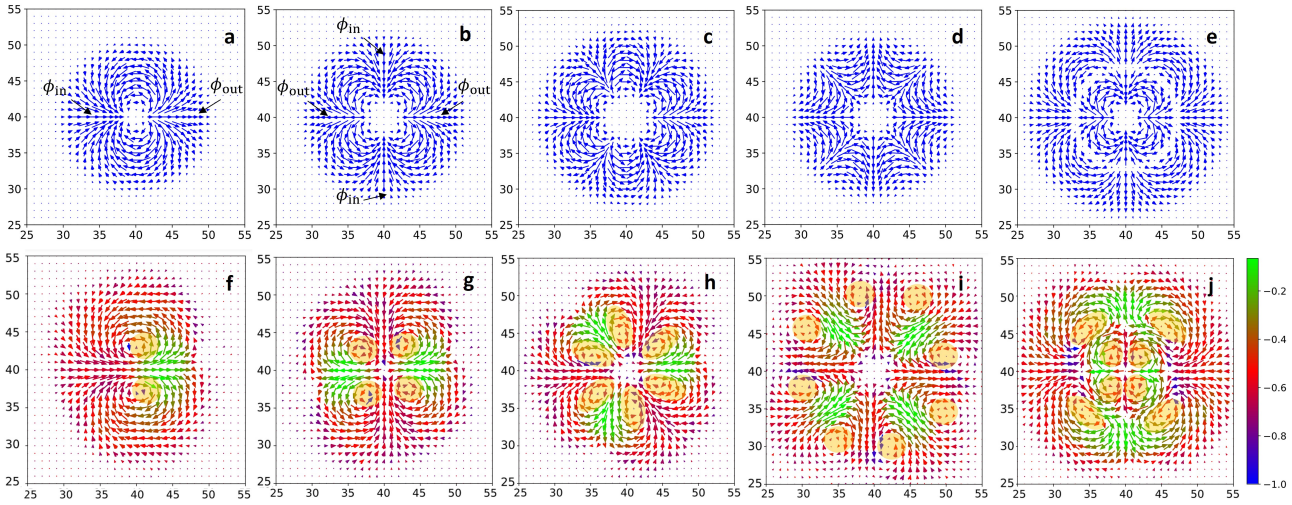


FIG. 1. Display of electric field patterns of various LG beams (first line) and of corresponding polar vortex arrays (second line) at $t = pT$. The x and y axes correspond to site numbers along two in-plane directions of the film. **a-d** $l = 0, m = -2,\ -3,\ -4,\ 3$. **e** $l = 1, m = -3$. $\phi_{\rm in}$ and $\phi_{\rm out}$ denoting the respective azimuthal angles of ingoing and outgoing fields are highlighted by arrows in **a** and **b**. In **d**, electric field displays as an antivortex at the center of the plane. **f-j** Polar vortex arrays formed under corresponding LG beams in the first line (in the order of **a-e**). The out-of-plane, P_z-component is normalized and denoted with the colorbar. The core of each vortex is highlighted in the yellow shaded area.

The maximal magnitude $E_{\rm max}$ for different l, m is set with respect to an experimental value at the order of 10^8 V/m [48, 49]. Computational methods and details can be referred to the supplementary material [50].

Figures 1(f)-(h) display the respective polar textures at the bottom (001) layer captured at approximate $t = pT$ after dipoles establish a cyclic motion since fields shown in Figs. 1(a)-(c) are introduced to the system. A time delay of approximately 0.1 ps is needed for dipoles to fully align with field vectors (see Fig. S4 and relavant discussions in the supplementary material). In-plane components of polar textures resemble to electric fields in that they share similar winding patterns and the same 2-dimensional $D_{|m|+1}$ symmetry. Side view plots shown in Fig. S1 in the supplementary material reveal that the magnitude of P_x developed in the central region is comparable to that of P_z in the poled monodomain. Nevertheless, differences between dipoles and fields are notable: rather than strictly adhering to the orientation of the on-site field and adopting a flux-closure pattern, dipoles arrange their orientations and form a vortex in each subregion! For example, in the case of $m = -2$ (Fig. 1(f)), dipoles at $x = 40, y = 41$ and 42 point along $+x$ direction and are antiparallel to dipoles at $x = 40, y > 43$ (e.g., $\phi = \frac{\pi}{2}$), while all corresponding field vectors at this azimuthal angle point along $-x$ direction (Fig. 1(a)). In another case of $m = -3$ (Fig. 1(g)), in the yellow shaded area within each quadrant, four neighboring dipoles change their orientations continuously and overall rotate by 2π and exhibit as the center of the vortex located in each quadrant, while corresponding field vectors in Fig. 1(b) only differ by an angle less than $\frac{\pi}{2}$. Note with an increasing $|m|$, domains confined by $\phi_{\rm in}$ and $\phi_{\rm out}$ get narrower along the azimuthal direction, while vortex in each domain extend along the radial direction, as illustrated in the case of $m = -4$ shown in Fig. 1(h). In all cases, dictated by orientations of field vectors on the boundary of each domain, neighboring vortices display opposite chiralities. Note that the generation of polar vortex array remains robust even with a one-order-magnitude-reduction in the field magnitude (see Fig. S3 in the supplementary material [50]).

Emergence of polar vortices can be explained as follows. At sites where electric field E_i are relatively large, the electrostatic energy $-\boldsymbol{E}_i \cdot \boldsymbol{p}_i$ is the dominant term; dipoles thus tend to align with the on-site electric field in order to minimize the electrostatic energy part introduced by light and reduce the total energy. In contrast, in the region where E_i are small, other energy contributions, including polarization gradient and polarization anisotropy [51], compete with the electrostatic energy; such anisotropy energy can be lowered by a progressive rotation of the polarization [18]. Additionally, when $r \to 0$, the orientation of the field undergoes a significant alteration owing to the factor of $m\phi$, despite the field magnitude $E \to 0$. If in-plane components of p_i align with E_i at $r \to 0$, a large bound charge $\rho_{\rm b}$ resulting from $\boldsymbol{\nabla} \cdot \boldsymbol{P}$ will be created in the central region, which will substantially increase the electrostatic energy [52, 53]. Taken together, this gives rise to the formation of vortices, where dipoles change their orientations continuously and form closed loops within each subregion. This is consistent with nanodomains in ferroelectric ultrathin films, where vortices emerge to preserve the

charge neutralities at surfaces and to reduce the electrostatic energy associated with the depolarization field and the anisotropy energy [24, 37, 54, 55]. For reference, without showing energy relevant to phenomenological models, different energy terms in effective Hamiltonian based on atomistic models, including on-site soft mode energies, short-range interaction energies, elastic energies, elastic-soft-mode coupling energies, dipole-dipole interaction energies, and electrostatic energies from coupling to the external field, have been plotted versus time in Fig. S2 in the supplementary material.

When considering positive m, a dipolar antivortex with notable in-plane components emerges in response to the anticrossing electric field, while $2(|m|+1)$ vortices are distributed in each sector of the antivortex (see Fig. 1(i) for $l=0, m=3$). As vortices are located relatively distant from the center, the local electric fields are comparably smaller, resulting in constituent dipoles of vortices possessing minor in-plane components. Nevertheless, these modest in-plane components manage to organize in a closed loop, giving rise to the formation of vortices. Figure 1(j) illustrates the dipolar pattern for $l=1, m=-3$. For nodal index $l=1$, an additional ring of vortices emerges at a greater radius, encircling the inner vortex array of $l=0$. The emerging ring of vortices consists of four elliptical vortices, aligning with the region where the field intensity approaches zero (also in a ring-like shape). Consistent with the preceding analysis, dipoles within this region can robustly adapt their orientations and manage to form a closed loop alongside the significant but antiparallel in-plane dipoles inside and outside the ring-like area. The self-organized and widely distributed vortex textures highlight the importance of polarization gradient and anisotropy energy among all competing energy contributions.

We next focus on the out-of-plane ($z-$) components of vortices. While all $z-$components are negative across the plane, their magnitudes vary by locations and depend on the on-site in-plane ($x-, y-$) components. Since only $P_{x,y}$ are directly coupled with light, P_z varies more as a response to $P_{x,y}$ to ensure a small bound charge $\rho_{\rm b}$, which is the sum of $\rho_{{\rm b},xy}$ and $\rho_{{\rm b},z}$. These two latter charges are the divergence to P_x+P_y and P_z, respectively. In a previous study, an LG beam with $l=0, m=-1$ induced the creation of 'Neel'-type skyrmions at specific times, of which P_z near the plane center switch their negative values to positive values [30]. The switching results from the convergent or divergent form of $E_{x,y}$ as well as $P_{x,y}$, and that causes a large bound charge $\rho_{{\rm b},xy}$ emerging at the center. To reduce the overall $\rho_{\rm b}$, P_z varies drastically so that $\rho_{{\rm b},z}$ can compensate $\rho_{{\rm b},xy}$. For $m\neq -1$, the chiral pattern of $E_{x,y}$ and $P_{x,y}$ exhibit divergence-free behaviors and only a small $\rho_{{\rm b},xy}$ is created. Therefore, a small $\rho_{{\rm b},z}$ is induced and P_z can maintain their negative values and vary smoothly throughout the plane. Figures 2(a)(b)

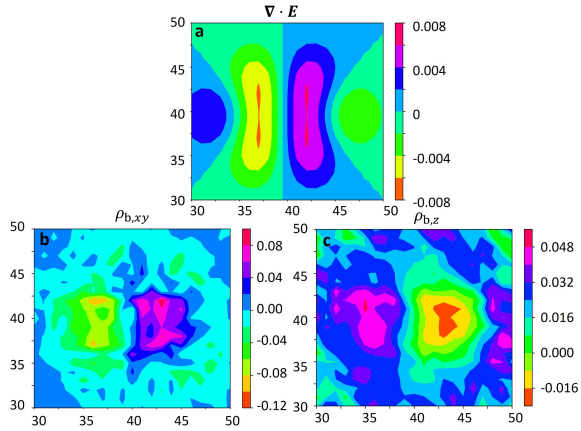


FIG. 2. The divergence of **a** electric field of LG beam with $l=0, m=-2$, **b** dipole components $P_{x,y}$ (which is bound charge component $\rho_{{\rm b},xy}$), and **c** P_z ($\rho_{{\rm b},z}$).

present the divergence of the electric field $\frac{\partial E_x}{\partial x}+\frac{\partial E_y}{\partial y}$ and the divergence of in-plane dipole components $\frac{\partial P_x}{\partial x}+\frac{\partial P_y}{\partial y}$ (namely, $\rho_{\rm b,xy}$) in the case of $l=0, m=-2$, respectively. As revealed in Figs. 1(a)(f), $P_{x,y}$ follows a pattern close to that of $E_{x,y}$, so the divergence of $E_{x,y}$ and of $P_{x,y}$ share similarities, featuring two regions with opposite values along x axis. This further induces a $\rho_{{\rm b},z}$ contrary to $\rho_{{\rm b},xy}$ in these regions (Fig. 2(c)), which finally determines that P_z at the (001) bottom layer adopt large negative values on the left side and small negative values on the right side of x axis. In areas in between, P_z undergoes a gradual variation as a transition.

Effective gyration of polar vortex arrays For a left-polarized LG beam, phases of electric field vectors increase by ωt as time progresses, leading to a conterclockwise rotation at each site. In addition, with a negative OAM value $m\neq -1$, the orienting angle of the on-site electric field vector increases with the azimuthal angle ϕ as $-m\phi$. Consequently, electric field vectors situated at larger ϕ at earlier times will align similarly to vectors situated at smaller ϕ at later time, resulting in an overall appearance of a "clockwise rotation" of the entire field pattern. Former studies already demonstrated that LG beam can trap or displace a single particle by gradient or scattering force [2–4]; now we wonder whether this dynamical feature of optical fields can be utilized to "spin" dipolar textures by driving a collective motion. Dipoles reside continuously over the lattice so every dipole interacts with the on-site field across the entire plane. Also, dipoles can reorient their directions readily to the dynamical field at THz frequency at all times. Thus, the "progressive rotation" belonging to the dynamical optical field, can be reproduced in vortex array.

Figures 3(a)-(d) present in-plane view about the polar vortex array corresponding to $l=0, m=-2$ at four different times starting from $t=nT$ to $t=(n+\frac{3}{4})T$ with

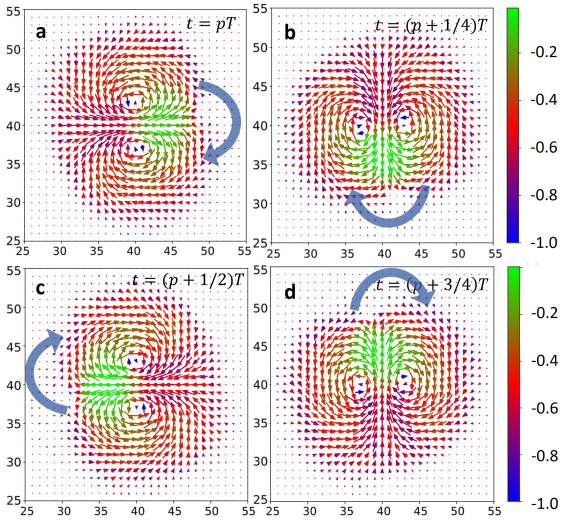


FIG. 3. The displayed dipole pattern for $l = 0, m = -2$ at different times t, as written in each panel. Yellow arrows denote the rotation direction of polar vortex arrays.

an interval of $\frac{1}{4}T$. We use similar notions ϕ_{in} and ϕ_{out} as we use for electric field in Fig. 1, to denote azimuthal angles where in-plane dipole components point radially inward or outward, respectively. The sequence of snapshots witnesses a complete gyration of the vortex array by an angle of 2π within a single period T, marked by the variation $\Delta\phi_{\text{in/out}} = \frac{\pi}{2}$ within an interval of $\frac{T}{4}$. Taking the distance from the vortex core to the center of the plane r_v as 3 u.c., the travelling speed of vortex array v can be approximated as $v = 2\pi r_v/T \approx 6000$ m/s, much faster than that of a magnetic skyrmion [32, 33].

It is evident that by adjusting the frequency ω and the chirality σ of the light, the gyration speed and its direction can also be modulated. Furthermore, we want to point out that there is an intrinsic connection between the gyration speed and OAM value m. A "complete" gyration refers to $\phi_{\text{in/out}}$ as the boundary of one subregion, moves to $\phi_{\text{in/out}}$ of the next subregion. Thus, based on Eq. 1, depending on m, a general expression of the gyration velocity can be given by:

$$v = \frac{2\pi r_v}{(-m-1)T}(m < 0), \quad v = -\frac{2\pi r_v}{(m+1)T}(m > 0). \quad (3)$$

This indicates that an LG beam with a lower value of m can actually spin vortex array more efficiently.

In summary, we demonstrate the idea of converting optical vortices to polar vortices in ferroelectric ultrathin films. Furthermore, the time evolution of a THz dynamical field induces a "gyration effect" of polar vortex arrays, causing them to rotate around the central axis at a speed synchronizing with the optical field. Our study presents an alternative scenario for creating electric vortices and manipulating their motions with optical signals.

Acknowledgement—We acknowledge the support from the Grant MURI ETHOS W911NF-21-2-0162 from Army Research Office (ARO) and the Vannevar Bush Faculty Fellowship (VBFF) Grant No. N00014-20-1-2834 from the Department of Defense. We also acknowledge the computational support from the Arkansas High Performance Computing Center and HPCMP Pathfinder Award for computational resources.

[1] L. Allen, M. W. Beijersbergen, R. Spreeuw, and J. Woerdman, Orbital angular momentum of light and the transformation of laguerre-gaussian laser modes, Physical Review A **45**, 8185 (1992).
[2] H. He, M. Friese, N. Heckenberg, and H. Rubinsztein-Dunlop, Direct observation of transfer of angular momentum to absorptive particles from a laser beam with a phase singularity, Physical Review Letters **75**, 826 (1995).
[3] M. Friese, J. Enger, H. Rubinsztein-Dunlop, and N. R. Heckenberg, Optical angular-momentum transfer to trapped absorbing particles, Physical Review A **54**, 1593 (1996).
[4] M. Dienerowitz, M. Mazilu, P. J. Reece, T. F. Krauss, and K. Dholakia, Optical vortex trap for resonant confinement of metal nanoparticles, Optics Express **16**, 4991 (2008).
[5] M. Padgett and R. Bowman, Tweezers with a twist, Nature Photonics **5**, 343 (2011).
[6] N. Simpson, L. Allen, and M. Padgett, Optical tweezers and optical spanners with laguerre–gaussian modes, Journal of Modern Optics **43**, 2485 (1996).
[7] D. G. Grier, A revolution in optical manipulation, Nature **424**, 810 (2003).
[8] K. Shintani, K. Taguchi, Y. Tanaka, and Y. Kawaguchi, Spin and charge transport induced by a twisted light beam on the surface of a topological insulator, Physical Review B **93**, 195415 (2016).
[9] A. Beekman, L. Rademaker, and J. van Wezel, An introduction to spontaneous symmetry breaking, SciPost Physics Lecture Notes , 011 (2019).
[10] J. M. Kosterlitz and D. J. Thouless, Ordering, metastability and phase transitions in two-dimensional systems, Journal of Physics C: Solid State Physics **6**, 1181 (1973).
[11] N. D. Mermin, The topological theory of defects in ordered media, Reviews of Modern Physics **51**, 591 (1979).
[12] D. Bishop and J. Reppy, Study of the superfluid transition in two-dimensional he 4 films, Physical Review Letters **40**, 1727 (1978).
[13] G. Blatter, M. V. Feigel'man, V. B. Geshkenbein, A. I. Larkin, and V. M. Vinokur, Vortices in high-temperature superconductors, Reviews of Modern Physics **66**, 1125 (1994).
[14] T. Shinjo, T. Okuno, R. Hassdorf, K. Shigeto, and T. Ono, Magnetic vortex core observation in circular dots of permalloy, Science **289**, 930 (2000).
[15] A. Wachowiak, J. Wiebe, M. Bode, O. Pietzsch, M. Morgenstern, and R. Wiesendanger, Direct observation of internal spin structure of magnetic vortex cores, Science **298**, 577 (2002).
[16] H. Fu and L. Bellaiche, Ferroelectricity in barium ti-

tanate quantum dots and wires, Physical Review Letters **91**, 257601 (2003).
[17] I. I. Naumov, L. Bellaiche, and H. Fu, Unusual phase transitions in ferroelectric nanodisks and nanorods, Nature **432**, 737 (2004).
[18] A. Yadav, C. Nelson, S. Hsu, Z. Hong, J. Clarkson, C. Schlepütz, A. Damodaran, P. Shafer, E. Arenholz, L. Dedon, *et al.*, Observation of polar vortices in oxide superlattices, Nature **530**, 198 (2016).
[19] P. Shafer, P. García-Fernández, P. Aguado-Puente, A. R. Damodaran, A. K. Yadav, C. T. Nelson, S.-L. Hsu, J. C. Wojdeł, J. Íñiguez, L. W. Martin, *et al.*, Emergent chirality in the electric polarization texture of titanate superlattices, Proceedings of the National Academy of Sciences **115**, 915 (2018).
[20] A. K. Yadav, K. X. Nguyen, Z. Hong, P. García-Fernández, P. Aguado-Puente, C. T. Nelson, S. Das, B. Prasad, D. Kwon, S. Cheema, *et al.*, Spatially resolved steady-state negative capacitance, Nature **565**, 468 (2019).
[21] I. Dzyaloshinsky, A thermodynamic theory of "weak" ferromagnetism of antiferromagnetics, Journal of Physics and Chemistry of Solids **4**, 241 (1958).
[22] T. Moriya, Anisotropic superexchange interaction and weak ferromagnetism, Physical review **120**, 91 (1960).
[23] S. Chen, S. Yuan, Z. Hou, Y. Tang, J. Zhang, T. Wang, K. Li, W. Zhao, X. Liu, L. Chen, *et al.*, Recent progress on topological structures in ferroic thin films and heterostructures, Advanced Materials **33**, 2000857 (2021).
[24] J. Junquera, Y. Nahas, S. Prokhorenko, L. Bellaiche, J. Íñiguez, D. G. Schlom, L.-Q. Chen, S. Salahuddin, D. A. Muller, L. W. Martin, *et al.*, Topological phases in polar oxide nanostructures, Reviews of Modern Physics **95**, 025001 (2023).
[25] A. R. Damodaran, J. Clarkson, Z. Hong, H. Liu, A. K. Yadav, C. T. Nelson, S.-L. Hsu, M. McCarter, K.-D. Park, V. Kravtsov, *et al.*, Phase coexistence and electric-field control of toroidal order in oxide superlattices, Nature Materials **16**, 1003 (2017).
[26] P. Behera, M. A. May, F. Gómez-Ortiz, S. Susarla, S. Das, C. T. Nelson, L. Caretta, S.-L. Hsu, M. R. McCarter, B. H. Savitzky, *et al.*, Electric field control of chirality, Science Advances **8**, eabj8030 (2022).
[27] V. Stoica, N. Laanait, C. Dai, Z. Hong, Y. Yuan, Z. Zhang, S. Lei, M. McCarter, A. Yadav, A. Damodaran, *et al.*, Optical creation of a supercrystal with three-dimensional nanoscale periodicity, Nature Materials **18**, 377 (2019).
[28] Q. Li, V. A. Stoica, M. Paściak, Y. Zhu, Y. Yuan, T. Yang, M. R. McCarter, S. Das, A. K. Yadav, S. Park, *et al.*, Subterahertz collective dynamics of polar vortices, Nature **592**, 376 (2021).
[29] T. Yang, C. Dai, Q. Li, H. Wen, and L.-Q. Chen, Condensation of collective polar vortex modes, Physical Review B **103**, L220303 (2021).
[30] L. Gao, S. Prokhorenko, Y. Nahas, and L. Bellaiche, Dynamical control of topology in polar skyrmions via twisted light, Physical Review Letters **132**, 026902 (2024).
[31] H. Fujita and M. Sato, Encoding orbital angular momentum of light in magnets, Physical Review B **96**, 060407 (2017).
[32] W. Yang, H. Yang, Y. Cao, and P. Yan, Photonic orbital angular momentum transfer and magnetic skyrmion rotation, Optics Express **26**, 8778 (2018).
[33] S. Guan, Y. Liu, Z. Hou, D. Chen, Z. Fan, M. Zeng, X. Lu, X. Gao, M. Qin, and J.-M. Liu, Optically controlled ultrafast dynamics of skyrmion in antiferromagnets, Physical Review B **107**, 214429 (2023).
[34] W. Zhong, D. Vanderbilt, and K. Rabe, Phase transitions in $BaTiO_3$ from first principles, Physical Review Letters **73**, 1861 (1994).
[35] W. Zhong, D. Vanderbilt, and K. Rabe, First-principles theory of ferroelectric phase transitions for perovskites: The case of $BaTiO_3$, Physical Review B **52**, 6301 (1995).
[36] P. Ghosez and J. Junquera, Modeling of ferroelectric oxide perovskites: From first to second principles, Annual Review of Condensed Matter Physics **13**, 325 (2022).
[37] I. Kornev, H. Fu, and L. Bellaiche, Ultrathin films of ferroelectric solid solutions under a residual depolarizing field, Physical Review Letters **93**, 196104 (2004).
[38] B.-K. Lai, I. Ponomareva, I. Naumov, I. Kornev, H. Fu, L. Bellaiche, and G. Salamo, Electric-field-induced domain evolution in ferroelectric ultrathin films, Physical Review Letters **96**, 137602 (2006).
[39] Y. Nahas, S. Prokhorenko, L. Louis, Z. Gui, I. Kornev, and L. Bellaiche, Discovery of stable skyrmionic state in ferroelectric nanocomposites, Nature Communications **6**, 1 (2015).
[40] A. Gruverman, D. Wu, H. Fan, I. Vrejoiu, M. Alexe, R. Harrison, and J. Scott, Vortex ferroelectric domains, Journal of Physics: Condensed Matter **20**, 342201 (2008).
[41] B. Rodriguez, X. Gao, L. Liu, W. Lee, I. Naumov, A. Bratkovsky, D. Hesse, and M. Alexe, Vortex polarization states in nanoscale ferroelectric arrays, Nano letters **9**, 1127 (2009).
[42] Y. Ivry, D. Chu, J. Scott, and C. Durkan, Flux closure vortexlike domain structures in ferroelectric thin films, Physical Review Letters **104**, 207602 (2010).
[43] Q. Zhang, L. Xie, G. Liu, S. Prokhorenko, Y. Nahas, X. Pan, L. Bellaiche, A. Gruverman, and N. Valanoor, Nanoscale bubble domains and topological transitions in ultrathin ferroelectric films, Advanced Materials **29**, 1702375 (2017).
[44] Y. Nahas, S. Prokhorenko, J. Fischer, B. Xu, C. Carrétéro, S. Prosandeev, M. Bibes, S. Fusil, B. Dkhil, V. Garcia, *et al.*, Inverse transition of labyrinthine domain patterns in ferroelectric thin films, Nature **577**, 47 (2020).
[45] H. Morioka, G. Asano, T. Oikawa, H. Funakubo, and K. Saito, Large remanent polarization of 100% polar-axis-oriented epitaxial tetragonal pb (zr 0.35 ti 0.65) o 3 thin films, Applied Physics Letters **82**, 4761 (2003).
[46] I. Vrejoiu, G. Le Rhun, L. Pintilie, D. Hesse, M. Alexe, and U. Gösele, Intrinsic ferroelectric properties of strained tetragonal pbzr0. 2ti0. 8o3 obtained on layer–by–layer grown, defect–free single–crystalline films, Advanced materials **18**, 1657 (2006).
[47] H. N. Lee, S. M. Nakhmanson, M. F. Chisholm, H. M. Christen, K. M. Rabe, and D. Vanderbilt, Suppressed dependence of polarization on epitaxial strain in highly polar ferroelectrics, Physical review letters **98**, 217602 (2007).
[48] B. Xu, J. Íñiguez, and L. Bellaiche, Designing lead-free antiferroelectrics for energy storage, Nature Communications **8**, 1 (2017).

[49] Z. Jiang, Y. Nahas, S. Prokhorenko, S. Prosandeev, D. Wang, J. Íñiguez, and L. Bellaiche, Giant electrocaloric response in the prototypical Pb(Mg, Nb)O_3 relaxor ferroelectric from atomistic simulations, Physical Review B **97**, 104110 (2018).

[50] See Supplemental Material [url] for computational details and methods, origins of skyrmion formation, and critical conditions and robustness of polar skyrmions, which includes Refs. [56–91].

[51] G. Catalan, J. Seidel, R. Ramesh, and J. F. Scott, Domain wall nanoelectronics, Reviews of Modern Physics **84**, 119 (2012).

[52] F. De Guerville, I. Luk'yanchuk, L. Lahoche, and M. El Marssi, Modeling of ferroelectric domains in thin films and superlattices, Materials Science and Engineering: B **120**, 16 (2005).

[53] I. A. Luk'yanchuk, L. Lahoche, and A. Sené, Universal properties of ferroelectric domains, Physical Review Letters **102**, 147601 (2009).

[54] I. Ponomareva, I. Naumov, I. Kornev, H. Fu, and L. Bellaiche, Atomistic treatment of depolarizing energy and field in ferroelectric nanostructures, Physical Review B **72**, 140102 (2005).

[55] I. Ponomareva, I. Naumov, and L. Bellaiche, Low-dimensional ferroelectrics under different electrical and mechanical boundary conditions: Atomistic simulations, Physical Review B **72**, 214118 (2005).

[56] S. Prosandeev, S. Prokhorenko, Y. Nahas, J. Grollier, D. Talbayev, B. Dkhil, and L. Bellaiche, Ultrafast activation and tuning of topological textures in ferroelectric nanostructures, Advanced Electronic Materials **8**, 2200808 (2022).

[57] L. Nordheim, Zur elektronentheorie der metalle. i, Annalen der Physik **401**, 607 (1931).

[58] A. Garcia and D. Vanderbilt, Electromechanical behavior of $BaTiO_3$ from first principles, Applied Physics Letters **72**, 2981 (1998).

[59] B.-K. Lai, I. Ponomareva, I. Kornev, L. Bellaiche, and G. Salamo, Thickness dependency of 180° stripe domains in ferroelectric ultrathin films: A first-principles-based study, Applied Physics Letters **91**, 152909 (2007).

[60] L. Bellaiche, A. García, and D. Vanderbilt, Low-temperature properties of $Pb(Zr_{1-x}Ti_x)O_3$ solid solutions near the morphotropic phase boundary, Ferroelectrics **266**, 41 (2002).

[61] M. H. Kwak, S. B. Kang, K.-C. Kim, S. Y. Jeong, S. Kim, B. H. Yoo, D. C. Chung, H. C. Ryu, D. S. Jun, M. C. Paek, *et al.*, Dielectric characteristics of Pb(Zr,Ti)O_3 films on MgO single crystal substrate by terahertz time domain spectroscopy, Ferroelectrics **422**, 19 (2011).

[62] S. W. Ko, W. Zhu, C. Fragkiadakis, T. Borman, K. Wang, P. Mardilovich, and S. Trolier-McKinstry, Improvement of reliability and dielectric breakdown strength of nb-doped lead zirconate titanate films via microstructure control of seed, Journal of the American Ceramic Society **102**, 1211 (2019).

[63] K. Y. Yun, D. Ricinschi, T. Kanashima, M. Noda, and M. Okuyama, Giant ferroelectric polarization beyond 150 μc/cm2 in bifeo3 thin film, Japanese journal of applied physics **43**, L647 (2004).

[64] N. J. Ramer and A. M. Rappe, Application of a new virtual crystal approach for the study of disordered perovskites, Journal of Physics and Chemistry of Solids **61**, 315 (2000).

[65] R. W. Heeres and V. Zwiller, Subwavelength focusing of light with orbital angular momentum, Nano Letters **14**, 4598 (2014).

[66] A. Toma, S. Tuccio, M. Prato, F. De Donato, A. Perucchi, P. Di Pietro, S. Marras, C. Liberale, R. Proietti Zaccaria, F. De Angelis, *et al.*, Squeezing terahertz light into nanovolumes: nanoantenna enhanced terahertz spectroscopy (nets) of semiconductor quantum dots, Nano Letters **15**, 386 (2015).

[67] D. Edwards, N. Browne, K. M. Holsgrove, A. B. Naden, S. O. Sayedghaee, B. Xu, S. Prosandeev, D. Wang, D. Mazumdar, M. Duchamp, *et al.*, Giant resistive switching in mixed phase $BiFeO_3$ via phase population control, Nanoscale **10**, 17629 (2018).

[68] Y. Nahas, S. Prokhorenko, Q. Zhang, V. Govinden, N. Valanoor, and L. Bellaiche, Topology and control of self-assembled domain patterns in low-dimensional ferroelectrics, Nature Communications **11**, 1 (2020).

[69] P. Chen, C. Paillard, H. J. Zhao, J. Íñiguez, and L. Bellaiche, Deterministic control of ferroelectric polarization by ultrafast laser pulses, Nature Communications **13**, 2566 (2022).

[70] V. Garcia and M. Bibes, Ferroelectric tunnel junctions for information storage and processing, Nature Communications **5**, 1 (2014).

[71] A. Chanthbouala, A. Crassous, V. Garcia, K. Bouzehouane, S. Fusil, X. Moya, J. Allibe, B. Dlubak, J. Grollier, S. Xavier, *et al.*, Solid-state memories based on ferroelectric tunnel junctions, Nature Nanotechnology **7**, 101 (2012).

[72] D. K. Gramotnev and S. I. Bozhevolnyi, Plasmonics beyond the diffraction limit, Nature Photonics **4**, 83 (2010).

[73] L. Novotny and N. Van Hulst, Antennas for light, Nature Photonics **5**, 83 (2011).

[74] V. Garcia, S. Fusil, K. Bouzehouane, S. Enouz-Vedrenne, N. D. Mathur, A. Barthelemy, and M. Bibes, Giant tunnel electroresistance for non-destructive readout of ferroelectric states, Nature **460**, 81 (2009).

[75] A. Rusina, M. Durach, K. A. Nelson, and M. I. Stockman, Nanoconcentration of terahertz radiation in plasmonic waveguides, Optics Express **16**, 18576 (2008).

[76] F. Mayer, M. Deluca, and M. N. Popov, Hidden phases in homovalent and heterovalent substituted $BaTiO_3$, Physical Review B **107**, 184307 (2023).

[77] L. Bellaiche and D. Vanderbilt, Virtual crystal approximation revisited: Application to dielectric and piezoelectric properties of perovskites, Physical Review B **61**, 7877 (2000).

[78] L. Bellaiche, A. García, and D. Vanderbilt, Electric-field induced polarization paths in $Pb(Zr_{1-x}Ti_x)O_3$ alloys, Physical Review B **64**, 060103 (2001).

[79] A. Schilling, T. Adams, R. Bowman, J. Gregg, G. Catalan, and J. Scott, Scaling of domain periodicity with thickness measured in $BaTiO_3$ single crystal lamellae and comparison with other ferroics, Physical Review B **74**, 024115 (2006).

[80] I. Ponomareva and L. Bellaiche, Nature of dynamical coupling between polarization and strain in nanoscale ferroelectrics from first principles, Physical review letters **101**, 197602 (2008).

[81] H. Béa, B. Dupé, S. Fusil, R. Mattana, E. Jacquet, B. Warot-Fonrose, F. Wilhelm, A. Rogalev, S. Petit,

V. Cros, *et al.*, Evidence for room-temperature multiferroicity in a compound with a giant axial ratio, Physical review letters **102**, 217603 (2009).
[82] D. Sichuga and L. Bellaiche, Epitaxial Pb(Zr,Ti)O_3 ultrathin films under open-circuit electrical boundary conditions, Physical Review Letters **106**, 196102 (2011).
[83] R. Mankowsky, A. von Hoegen, M. Först, and A. Cavalleri, Ultrafast reversal of the ferroelectric polarization, Physical Review Letters **118**, 197601 (2017).
[84] L. Lu, Y. Nahas, M. Liu, H. Du, Z. Jiang, S. Ren, D. Wang, L. Jin, S. Prokhorenko, C.-L. Jia, *et al.*, Topological defects with distinct dipole configurations in $PbTiO_3$/$SrTiO_3$ multilayer films, Physical Review Letters **120**, 177601 (2018).
[85] S. Prosandeev, J. Grollier, D. Talbayev, B. Dkhil, and L. Bellaiche, Ultrafast neuromorphic dynamics using hidden phases in the prototype of relaxor ferroelectrics, Physical Review Letters **126**, 027602 (2021).
[86] L. Bellaiche, A. García, and D. Vanderbilt, Finite-temperature properties of $Pb(Zr_{1-x}Ti_x)O_3$ alloys from first principles, Physical Review Letters **84**, 5427 (2000).
[87] S. t. Streiffer, J. Eastman, D. Fong, C. Thompson, A. Munkholm, M. R. Murty, O. Auciello, G. Bai, and G. Stephenson, Observation of nanoscale 180° stripe domains in ferroelectric $PbTiO_3$ thin films, Physical Review Letters **89**, 067601 (2002).
[88] C. Ederer and N. A. Spaldin, Effect of epitaxial strain on the spontaneous polarization of thin film ferroelectrics, Physical review letters **95**, 257601 (2005).
[89] G. Spektor, D. Kilbane, A. Mahro, B. Frank, S. Ristok, L. Gal, P. Kahl, D. Podbiel, S. Mathias, H. Giessen, *et al.*, Revealing the subfemtosecond dynamics of orbital angular momentum in nanoplasmonic vortices, Science **355**, 1187 (2017).
[90] M. Pu, X. Ma, Z. Zhao, X. Li, Y. Wang, H. Gao, C. Hu, P. Gao, C. Wang, and X. Luo, Near-field collimation of light carrying orbital angular momentum with bull's-eye-assisted plasmonic coaxial waveguides, Scientific Reports **5**, 1 (2015).
[91] D. Garoli, P. Zilio, Y. Gorodetski, F. Tantussi, and F. De Angelis, Optical vortex beam generator at nanoscale level, Scientific Reports **6**, 1 (2016).